Design and Validation of Medical Devices for Photothermally Augmented Treatments

Rudy Thomas Andriani, Jr.

Thesis submitted to the faculty of the Virginia Polytechnic Institute and State University
in partial fulfillment of the requirements for the degree of

Master of Science
In
Mechanical Engineering

Christopher G. Rylander, Chair
John L. Robertson
John H. Rossmeisl

August 15, 2014
Blacksburg, VA

Keywords: Convection-Enhanced Delivery, Carbon Nanohorn, Microneedle,

Design and Validation of Medical Devices for Photothermally Augmented Treatments

Rudy Thomas Andriani, Jr.

Abstract

1-Dimensional Advective-Diffusion Model in Porous Media

Infusion of therapeutic agents into tissue is makes use of two mass transport modes: advective transport, and molecular diffusion.

Bulk infusion into a 0.6% wt agarose phantom was modeled as an infinite, homogenous, and isotropic porous medium saturated with the same solvent used in the infused dye tracer. The source is assumed to be spherical and isotropic with constant flow rate and concentration. The Peclet numberdecreases with power function $Pe = 15762t^{0.337}$ due to the decrease in mean dye-front pore velocity as V goes to V_{final}.

Diffusive mass transport does not become significant during any relevent time period.

Arborizing Fiberoptic Microneedle Catheter

We have developed an arborizing catheter that allows multiple slender fused-silica CED cannulae to be deployed within a target volume of the brain via a single needle tract, and tested it in a widely accepted tissue phantom.

The arborizing catheter was constructed by bonding and encapsulating seven slender PEEK tubes in a radially symmetric bundle with a progressive helical angle along the length, then grinding a conicle tip where the helical angle is greatest.

The catheter was tested by casting 0.6% wt agarose around the device with all needles deployed to a tip-to-tip distance of 4 mm. Phantom temperature was maintained at 26 ± 2°C. 5% wt Indigo Carmine dye was infused at a rate of 0.3 uL/min/needle for 4 hours.

N=4 infusions showed a V_d/V_i of 139.774, with a standard deviation of 45.01. This is an order of magnitude greater than single-needle infusions under similar conditions [45]. The arborizer showed the additional benefit of arresting reflux propagating up the lengths of individual needles, which has historically been a weakness of single-needle CED catheter designs.

In Vivo Co-Delivery of Single Walled Carbon Nano-horns and Laser Light to Treat Human Transitional Cell Carcinoma of the Urinary Bladder in a Rodent Model

Using a rodent model we explored a treatment method for Transitional Cell Carcinoma (TCC) in the urinary bladder in which Single Walled Carbon Nanohorn (SWNH) solution and 1064 nm laser light are delivered into tumorous tissue via a co-delivery Fiberoptic Microneedle Device (FMD).

Preliminary treatment parameters were determined by injecting SWNH solutions with concentrations of 0 mg/mL, 0.17 mg/mL, or 0.255 mg/mL into ex vivo porcine skin and irradiating each for three minutes at laser powers of 500 mW, or 1000 mW. The combination with the greatest temperature increase without burning the tissue, 0.17 mg/mL at 1000 mW, was selected for the in vivo treatment.

TCC tumors were induced in a rodent model by injecting a solution of 10^6 AY27 urothelial carcinoma cells into the lateral aspect of the left hind leg of young, female F344 rats. When tumors reached 5-10 mm^3, rats were anesthitized and treated. SWNH solution was injected directly into the tumor and irradiated until the target temperature of 60degC was achieved. The rats were then recovered from anestesia and monitored for 7-14 days, at which point they were humanely sacrificed, and the tumors prepared for histological examination.

Histological assessment of areas of FMD treatment correlated well with gross morphological appearance. Foci of tumor necrosis showed sharp (1-2 mm) delineation from areas of viable tumor (not treated) and normal tissue.

We believe we have demonstrated the feasibility of using the FMD for treatment of urothelial carcinoma using an animal model of this disease, and are encouraged to continue development of this treatment and testing in larger animal models.

Acknowledgements

The tremendous amount of gratitude I have for so very many peoples' support, encouragement, advice, and faith is difficult for me to put into words, making this one of the only times I've ever wished I had majored in English.

Without my parents, Penny and Rudy Sr., my sister, Leslie, and Christine Ricucci behind me every step of the way, my sanity might be very much in question right now.

I would like to thank my advisor, Dr. Christopher Rylander, for his support and guidance throughout my academic pursuits, as well as my committee members Dr. John Robertson and Dr. John Rossmeisl for their guidance in the ways of academic research and career planning.

I would be remiss not to acknowledge the contributions of my classmates, collaborators, and friends, Katelyn, Bill, Matt, Allyson, Melissa, Laura, and many others.

And finally, a very special thanks to Dr. Lyle Hood for his friendship, guidance, and encouragement during some of the most critical points in this journey.

This research was funded by The Coulter Foundation Translational Research Award and the National Institute of Health Grant Number R21CA156078-02.

Chapter 4 post-mortem photographs and histological images by Dr. John L. Robertson.
All other images by author.

For My Wonderful Mother

Penny Anna Andriani

May 19, 1955 – July 21, 2014

Table of Contents

LIST OF FIGURES

List of Tables

Chapter 1: Introduction

1.1 Introduction of the Fiberoptic Microneedle Co-Delivery Device

Malignant tumors of the central nervous system are the third leading cause of cancer-related deaths in adolescents and adults between the ages of 15 and 34; in children, brain tumors are the leading cause of cancer death. Over the past several decades there has been a steady increase in the incidence of brain cancers and, given the aging population, brain tumors will soon be one of the most commonly encountered human neoplasms. Malignant Glioma (MGs) is the most common form of malignant tumor in the central nervous system, and is associated with a mean survival time post-diagnosis of 15 months and a mortality rate exceeding 95% [1]. Common approaches to the treatment of MGs involve surgical resection, radiation therapy, and chemotherapy, or combinations of these three modalities [2] [3]. Prior to the development of adjunctive therapy protocols combining radiation therapy and the chemotherapeutic drug, temozolomide, fewer than 5% of patients survived more than 2 years. However, neither single nor multimodality treatments are curative with the combination of adjunctive therapies improves survival by a few months to a rate of 26%[1]. At present, treatment of both primary and secondary brain tumors is provided to improve or sustain neurological function of the patient, to diminish the size of the tumor growing intracranially, and to lengthen intervals between treatments. One of the reasons for poor survival is that glioma cells typically infiltrate up to 2 cm beyond the volume of visible tumor, making them difficult to detect and treat. Treatment of MGs is also limited by insufficient delivery of chemotherapy drugs due to the blood/brain barrier. Thus, new specific methods of MG treatment are urgently needed.

Convection-enhanced delivery (CED) has emerged as a promising experimental method for combatting intracranial tumors through direct infusion of highly concentrated chemotherapeutics directly into the tumor volume [4], [5]. CED involves the stereotactically guided insertion of a small-caliber catheter into the brain parenchyma. Through this catheter, chemotherapeutic infusate is actively pumped (flow rates range from 1-10 μL/min) into the brain parenchyma and pushed through the interstitial space [6]. Infusion is continued for up to several days before catheters are removed at the bedside [6]. In contrast to the millimeter diffusion distances obtained with simple infusion, CED has been shown in laboratory experiments to deliver high-molecular-weight proteins 2 cm into the brain parenchyma after as little as 2 hours of continuous infusion[7]. This was accomplished without causing cerebral edema and was unaffected by capillary loss or metabolization of the macromolecule. With these initial experiments, CED was established as a viable method for providing regional distribution of molecules as large as immunotoxins and radioisotope–conjugated antibodies, and even some conventional chemotherapeutic agents [8-13]. Laser Induced Thermotherapy (LITT) is another relatively new technology used in treating neurological, liver, and other neoplasms or lesions [14,15].

Thermochemotherapy, a technique in which the chemotherapeutic agents are heated to sub-lethal temperatures, has been shown clinically and in laboratory studies to enhance fluid penetration into peritoneal tumors, as well as increase the cytotoxic effects of several chemotherapeutic drugs[16-18].

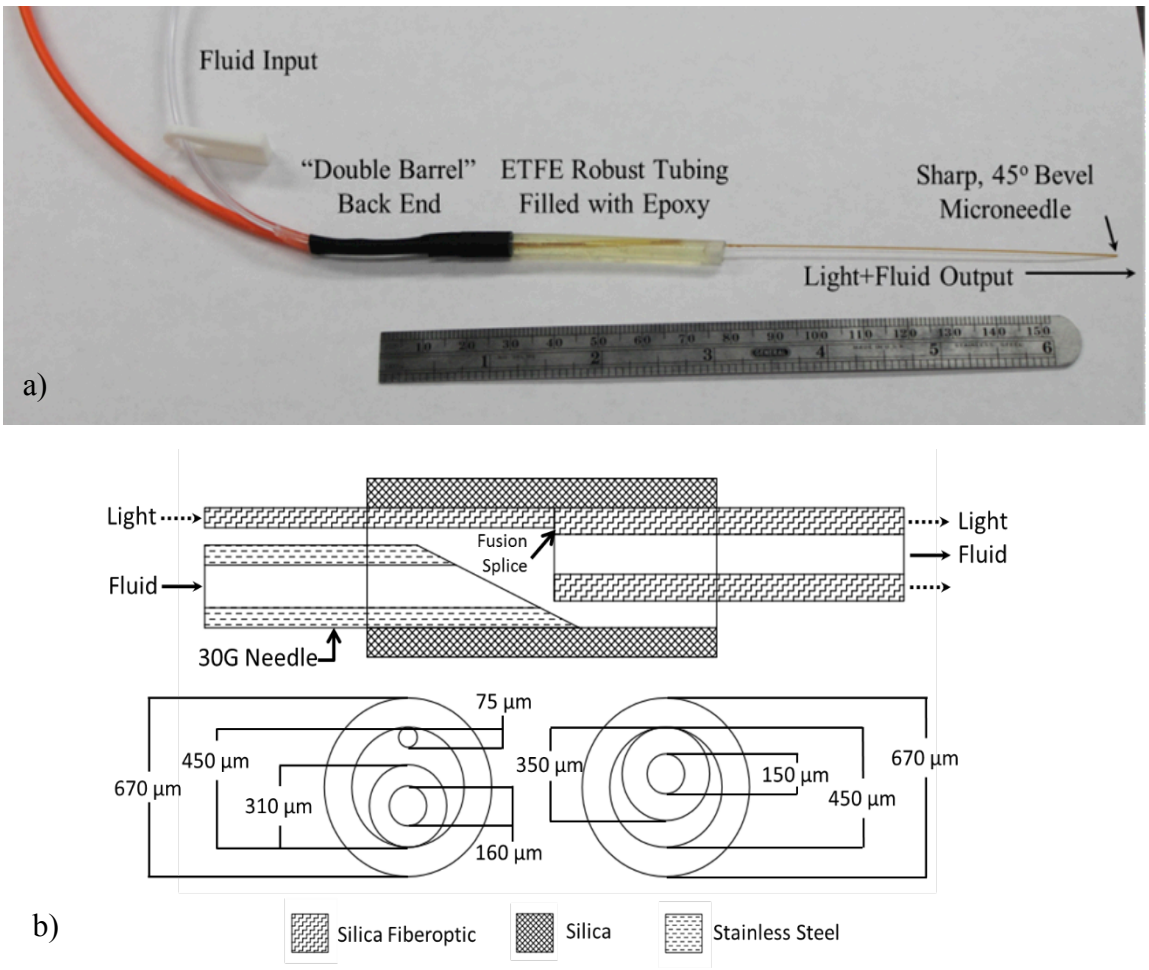

Figure 1-1: a) Current FMD Prototype. b) Schematic of FMD co-delivery couple design. R. L. Hood, J. H. Rossmeisl, R. T. Andriani, A. R. Wilkinson, J. L. Robertson, and C. G. Rylander, "Intracranial hyperthermia through local photothermal heating with a fiberoptic microneedle device," *Lasers Surg. Med.*, vol. 45, no. 3, pp. 167–174, Mar. 2013. Used under fair use, 2014.

While promising technologies, the brains heterogeneous nature, which is only amplified in the presence of a tumor, makes the distribution of CED's drugs, and LITT's thermal gradients very difficult to predict. As a result, cancerous tissue can be missed. Even if MR or CT scans no longer show a tumor, diseases such as Malignant Glioma (MG) can extend up to 2 cm beyond the visible tumor margins, thus making recurrence likely.

Our group has been developing a platform technology dubbed the 'Co-Delivery Couple' Fiberoptic Microneedle Device (FMD, for simplicity), which marries the best characteristics of these three techniques, while mitigating many of their disadvantages. The co-delivery couple enables the delivery of light, typically laser, via light conducting properties of the walls of certain fused-silica capillary tubes (Polymicro, Phoenix, AZ), and bulk fluids via the bore of the capillary tube. This is accomplished by fusion splicing a small multi-mode optical fiber to the annular core of a light-guiding fused-silica capillary tube, and enclosing the spliced section in a fluid-coupling sleeve.

We will be exploring the use of this device and techniques that will be able to take advantage of its properties in the near future here in this paper. Specifically, I will discuss a study validating a device and technique for further enhancing the effects of photothermally augmented convection enhanced delivery (CED) into parenchymal tissue in both tissue phantoms and preliminary *in vivo* experiments, as well as cytoscopic treatment of late-stage bladder cancers via direct intratumoral infusion and targeted photothermal heating of Single Walled Carbon Nanohorns (SWNH).

1.2 Introduction to the Arborizing Fiberoptic Microneedle Catheter

Often CED and LITT require multiple risky catheter insertions as a means of infusing or ablating a greater tissue volume [20, 21]. When a catheter or probe of some sort is inserted into a cancerous lesion the possibility of seeding the needle tract with cancer

cells or other diseased tissue exists despite the inclusion of the tract in the treatment protocol. Intuitively, the more insertions made into the lesion, the more likely a needle tract will be seeded. Similarly, multiple insertions also increases the chance of critical neural pathways being disrupted. Common wisdom among neurosurgeons is that a single, larger catheter that can be guided through less critical volumes within the brain is preferable to multiple insertions of smaller catheters, even if the sum of their diameters does not exceed the larger catheter.

This paper will detail the development and validation of a device intended to mitigate these risks by enabling up to seven individual FMDs to be guided to a target volume via a single needle tract no larger than a standard 12G cannulus, and arborize them at up to a 30° angle into the target area, thereby providing multiple treatment points per primary catheter insertion that would otherwise require multiple risky insertions.

1.3 Introduction to the In Vivo Co-Delivery of Single Walled Carbon Nano-Horns and Laser Light to Treat Transitional Cell Carcinoma in a Rodent Model

Bladder cancer is the fourth most prevalent noncutaneous malignancy in the United States, with approximately 70,980 new cases in 2009 alone[22]. Approximately 30% of new diagnoses are already at an advanced clinical stage (stage 2-3), meaning the tumors have already penetrated into the muscular and serosal layers of the bladder, and metastasized to surrounding organs[23].

Treatment of these late stage cancers typically involves removal of the bladder, and possibly other adjacent organs and structures, resulting in other chronic health problems and significant decrease in quality of life for the patient.

We have explored the use of the FMD for infusion and selective photothermal heating of Single Walled Carbon Nanohorns (SWNH) as a means of selectively destroying these later stage cancers in a far less intrusive manner.

Chapter 2: 1-Dimensional Advective-Diffusion Model in Porous Media

2.1 Introduction

Infusion of therapeutic agents into tissue makes use of two mass transport modes: Advective transport of a solute, and molecular diffusion of a solute from areas of high concentration to areas of low concentration. This section will explore the theory behind the combined advective diffusion of CED and illustrate why advection is the dominant transport mode.

2.2 Theory

Bulk Flow through Porous Media

When discussing bulk transport through porous media, it should be noted that a great deal of work is based on Darcy's Law, which is the result of some of the first work exploring single-phase transport phenomena in porous media [24, 25]. Its original form,

$$k\Delta \mathrm{p} = \mathrm{Ue}, \tag{2.1}$$

was derived from a primitive sand-based water filtration apparatus [24] (Figure 2.x). As a result, it is only valid for incompressible, isothermal creeping flow of a Newtonian fluid through a long, uniform, isotropic porous medium of low hydraulic conductivity [24]. However, by modifying Darcy's law slightly and applying a modified continuity equation, X. Chen *et al.* [26] have shown that infusions into agarose hydrogel tissue

phantoms, such as those discussed in later chapters, can be suitably modeled as infusions into rigid porous media. Z. Chen *et al.* [27], in turn, have shown that similar agarose hydrogels, albeit of slightly lower concentration and therefor higher porosity, are suitable as realistic brain tissue phantoms for such infusion studies [27].

Fick's Law

The simplest mode of mass transport in a fluid medium is molecular diffusion. In a motionless fluid, solute in an initial volume, V, undergoes Brownian motion, thereby increasing or decreasing the volumetric concentration, c(**r**,t), of a given solute within V, assuming the solute concentration in question is not in equilibrium. Fick's law relates this concentration gradient to the flux, **j**, of molecules relative to this volume by the equation

$$\boldsymbol{j} = -D\nabla c \tag{2.2}$$

Where D is the diffusion coefficient of the solute through the fluid, the value of which depends on the particular fluid and diffusive species, and is defined in units of $\frac{length^2}{time}$ [28].

When we introduce convective flow to the situation described above, eq.2.2 becomes the empirical flux law (eq. 2.3) by superposition.

$$\boldsymbol{j} = \boldsymbol{v}c - D\nabla \mathrm{c} \tag{2.3}$$

In dealing with porous media at the macroscopic scale, the pore fraction, or void space of the media, denoted as ϕ, must be taken into account, and can be done by introducing the pore fraction to the empirical flux law as shown here [29]:

$$\boldsymbol{j} = \phi \boldsymbol{v} c - \phi D \nabla c \tag{2.4}$$

Peclet Number

The relationship between the advective and diffusive mass transfer rates (advective vs. diffusive mass flux) is illustrated by a ratio known as the Peclet Number. It is defined as,

$$Pe = \frac{LU}{D}, \tag{2.5}$$

where L is the characteristic length of the volume $\frac{V_{body}}{A_{surface}}$, a sphere in our case, U is the bulk fluid velocity, and D is the coefficient of diffusion [30]. Pe$\ll$1 shows that molecular diffusion is the dominant mechanism, and Pe$\gg$1 shows advection to be the dominant mechanism, thus making it the ideal metric for our purposes.

2.3 Model

As discussed above, agarose has been shown to be a suitable non-biological phantom for experimental CED infusions because its transport properties are very similar to those of mammalian brain tissue. While the transport rate is not identical to that of brain tissue, V_d/V_i has been shown to scale linearly with non-perfused biological tissue, and so allows us to predict distribution [27]. The goal of the model is to show that advection is the dominant transport mechanism for infusions into agarose brain phantoms.

Methods

Table 2-1: Known Quantities

Property	Value
Pore Fraction (ϕ)	0.995
Source Concentration (C_0)	0.05
Source Flow Velocity (v)	$0.424\ \frac{\text{cm}}{min}$
Solute Effective Longitudinal Distribution Coefficient (D_L)	$0.378 * 10^{-9}\ \frac{cm^2}{min}$

The 0.6% wt agarose phantom was modeled as an infinite, homogenous, and isotropic porous medium saturated with the same solvent used in the dye tracer. The embedded source is assumed spherical and isotropic, with diameter equal to the 0.015 cm bore of our FMD catheter. Flow rate and solute concentration are constant at the source. Flow is assumed non-reactive and non-adsorbing. In keeping with the homogeneous, isotropic assumptions of the source and medium, the infusion volume is also assumed spherical. Since this is a bulk infusion model, the effect of micro-scale pore morphology is simply described by the homogeneous and isotropic assumptions.

Since we are dealing with porous media, *U* from eq. 2.4 becomes the mean pore velocity $\frac{v}{\phi}$, and the effective longitudinal distribution coefficient D_L is substituted in for diffusion coefficient *D*.[1]

[1] Estimated using $D_L = v_{DF}\overline{D_p}$, where $\overline{D_p}$ is the average solute spherical particle diameter approximation calculated from Indigo Carmine's molar volume, and v_{DF} is the average pore velocity as defined by the Dupuit-Forcheimer assumption [25].

The Peclet number for infusion timepoints from 1 to 240 minutes using the known quantities shown in Table 1.

2.4 Results

The Peclet number calculated at t=1 minute is on the order of 10^4, and decreases throughout the infusion. The Peclet number as a function of time, shown in Figure 2, is best described by power equation $Pe = 15762t^{0.337}$, as $R^2 = 0.9973$. The decrease in the Peclet number is due to the decrease in mean dye-front pore velocity as V goes to V_{final}. At the modeled flow rate, diffusive mass transport does not become significant during any relevent time period.

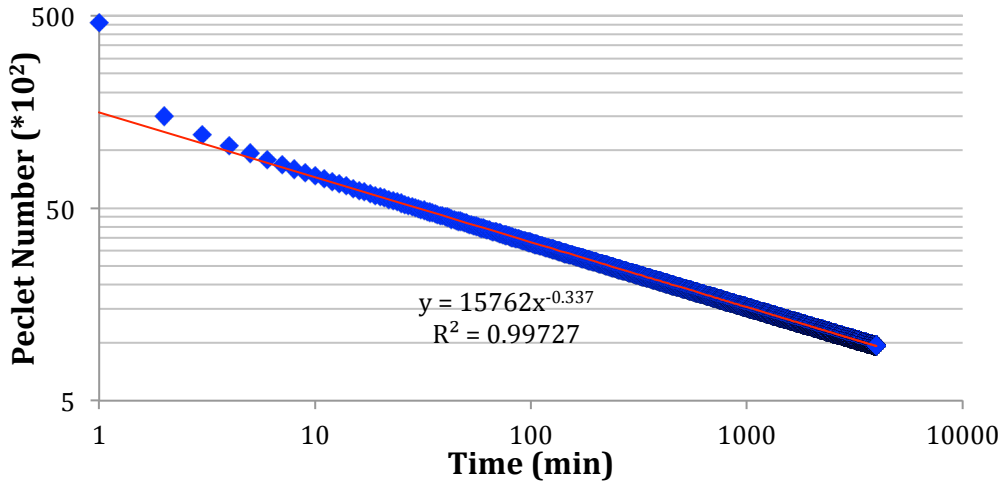

Figure 2-1: The Peclet number calculated for the modeled infusion rate as a function of volume.

Chapter 3: Arborizing Fiberoptic Microneedle Catheter

3.1 Introduction

Large tumors sometimes require multiple cannulae in order to infuse a sufficient tissue volume with the chemotherapeutic drug. However, even with small gauge cannulae the needle track is critical, as a poorly placed cannulus can sever critical neural connections. It is also possible to seed needle tracks with cancer cells when the cannulus is withdrawn. Multiple cannulae introduce the potential to seed multiple tracts through the brain [31]-[35]. A single larger gauge cannulus can be more easily guided through less critical volumes of the brain to the target region where the arborizor will deploy its needles. Reflux of the infusate during the treatment is also an issue inherent with CED treatments. While insertion tracts are sometimes included in the treatment area, reflux of the infusate along the needle tract decreases forward motion of the infusion into the brain, as well as increases the error in the measurement of how much infusate has been delivered to the target volume. The motivation of this study was to determine if such an arborizing design is feasible so that the co-delivery couple may be integrated into the design in the future.

3.2 Methods

Design Criteria

The following design criteria were established using current CED research and input from practicing clinicians. A maximum diameter of 3mm was established, which is comparable to a commercially available 11G brain biopsy needle. Materials must be MRI

compatible, and must be biocompatible in the final product. However, when biocompatible materials were not cost effective for prototyping purposes, less expensive materials were selected. Any materials used would need to withstand autoclave and/or ethylene oxide sterilization. In order to infuse clinically relevant volumes without the need to use excessively long needles, a target arborizing angle range (angle of peripheral needles from catheter axis) of 25° to 45° was established. The arborizer would need to deflect the needles to these angles while causing minimal mechanical stress on the needles. Two technical challenges inherent in CED are reflux of infusate up the exterior of the catheter, and clogging due to tissue coring upon insertion of catheters equipped with axial delivery ports. Since the current FMD design makes use of an axial port, each needle would need to have an individual pressure reservoir (i.e. one syringe pump per needle). In the event of a clogged FMD, a common pressure reservoir would cause the flow rate through the remaining needles to increase. With individual reservoirs, the pump to the clogged needle can simply be shut off without effecting the other infusions. Finally, a mechanism to arrest reflux of infusate should be included. Ideally, an arborizing design will decrease deleterious reflux since the fluid dispensing needles are deployed only within the tumor tissue. Any reflux would follow the dispensing needle tract up to the arborizing cannulas where a large, sudden increase in the size of the body the infusate is following can arrest the backflow. A similar effect has been demonstrated by Krauze *et al.* [36] with single CED catheters modified to include a step increase in diameter a short length from the catheter tip.

Function – Structure Summary

The required functions and sub-functions of the arborizer were listed and geometric features of the arborizer were catalogued using a Function-Structure design method. The function-structure table of the final design's primary features is summarized in Table 2.

Materials Selection

In this early stage of development, long-term biocompatibility of the materials used to construct the catheter was not a highly weighted priority. However, since experimentation and clinical use in an MRI is a primary goal of the project, every effort to avoid materials that would interfere with the function of an MRI was made. Polyetheretherketone (PEEK) is a high performance, non-reactive thermoplastic often used in high-pressure chromatography and orthopedic medical applications. Slender tubing (794 um OD, 381 um ID) is readily available (IDEX Health and Science), and capable of maintaining its structural integrity during the arborizer manufacturing process. Biocompatible epoxy in which to encapsulate the helical tube bundle is cost prohibitive this early in the development process. A suitable commercially available epoxy (2-Ton, Devcon, Danvers, MA) was selected due. Both materials are able to withstand standard medical sterilization techniques.

Table 3-1: Arborizer Function-Structure Summary

Function	Structure
Provide Lateral Support to Needles	• Close Tolerance Guide Tubes
Provide 25° to 45° of deflection	• Helical Tubing Configuration
Protect needles during catheter insertion	• Needles can fully retract into catheter, or be inserted after catheter is in position.
Allow smooth needle actuation	• Close Tolerance Guide Tubes • Helical Tubing Configuration
Maintain needle's axial position	• Close Tolerance Guide Tubes • Helical Tubing Configuration
Arrest Reflux	• Step Increase in Geometry at Needle-Catheter interface
Minimize Disruption to Parenchimal Tissue	• Smooth Exterior • Concle Tip
Visible using Standard Medical Imaging Techniques	• Material Selection allows for visualization on MRI (void space) and CT (contrast)

Construction

Lengths fused silica fiber (Polymicro, FIP300330370) were inserted into shorter lengths of PEEK tubing for support. The tubing was abraded and bundled into sets of seven, and held in a radial symmetric configuration by a length of heat-shrink tubing (HST), approximately 1 cm in length, terminating approximately 10 cm from the end that will form the tip of the arborizer. Cyanoacrilate adhesive is applied to a 1 cm length of the tubes adjacent to the heat shrink tubing. The tubes are aligned and the adhesive allowed to cure. Once cured, the bonded section is braced with an additional 1 cm of HST. A 1.5 cm length of the tubing bundle is left exposed as another length of HST is exposed. As the HST cools, the bundle is twisted approximately 35°, and another coating of cyanoacrylate is applied. This process of bracing, twisting, and bonding the tubing is

repeated, applying an additional 70° rotation. At this point the bundle is braced with a double layer of HST, and the free ends of the bundle are inserted into an angle-spacing jig, where the final 145° twist is applied. Once the cyanoacrylate has cured, all HST except for the first, most distal, section is removed and the tubing is abraded again.

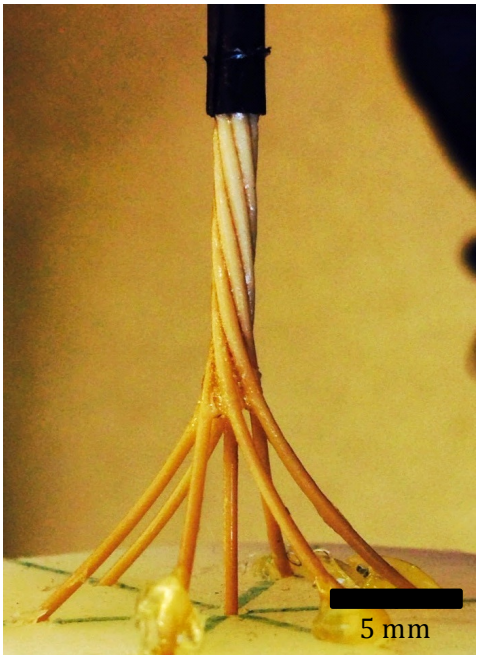

Figure 3-1: An arborizer prepared for exterior epoxy layer.

The bundle is sonicated to clear the exterior of debris, and then hung with the end distal to the jig ('the back-end') pointing toward the work surface. The epoxy is applied at a point just above the arborized tubing, and allowed to flow down over the body of the bundle. Heat is applied to reduce the viscosity of the epoxy, allowing for a thinner, more uniform exterior for the catheter. Once the epoxy has cured the arborizer was cut from the jig, and the 30° conical tip ground to shape using a lapping wheel with 60 μm lapping film. Any other irregularities in the surface were buffed out using the same grade of film.

Figure 3-2: Finished distal end of arborizer.

Depending on the intended application, the back-end was either ground flat to the level of the epoxy, or the extra tubing was fanned out and supported by a bracket for ease of needle manipulation by a gloved surgeon.

Testing and Validation

Agarose phantoms were cast in 8.5 cm cubic, transparent acrylic containers. The arboriser is epoxied into a 2.5 mm ID/ 12.5 mm OD acrylic tube for support, then inserted into a 3 mm hole drilled into a face of the container so that the tip is ~12 mm above the centroid of the container volume. The needles are inserted into the arborizer and deployed to a length of ~12.5 mm so that the tips are spaced 4 mm from each other. To prevent unwanted movement, they are hot-glued to the distal end of the arborizer. The

two halves of the container are assembled and the seams sealed with a flexible silicon sealant.

The needles were manufactured by cutting fused-silica capillary tubing (TSP150375, Polymicro Technologies, Phoenix, AZ) to lengths of 14 cm. The cut ends were cleared of debris, and one end inserted into the bore of a 22G dispensing needle with a Luer connector, and fixed in place with epoxy.

Care is taken to keep all seven needles at the same length from the Luer connector. This keeps variations in fluid resistance between needles low. Compliance in the fluid system would otherwise exacerbate the differences in infusion rates of individual needles during the transient period of the infusion.

The needles are then tested to ensure there are not leaks. A length of fused silica fiber (FIP100110125, Polymicro Technologies) is inserted into the bore of each needle to prevent clogging during the phantom casting process. The fiber is flush with the needle tip and extends beyond the Luer connector for easy removal. Water is then pushed through the remaining space within the bore in order to remove any air bubbles. A 3-way T-couple is then attached to each needle with the anti-clogging fiber extending through both coaxial ports, filled with water, and temporarily plugged the perpendicular port in order to prevent accidental drainage.

Agarose Gel (BioRad, Hercules, CA) is prepared by mixing agarose powder and deionized water in a 0.6% weight ratio in an Erlenmeyer flask. The mouth of the flask is

covered with aluminum foil to minimize evaporation losses, and heated on a hot plate to a low boil until the agarose powder has completely dissolved. The solution is allowed to cool for 15 minutes before being poured into the phantom container via one of the two access holes drilled in the top face of the cube. When the container is full, both access hole are rimmed with a small amount of latex sealant and then covered with paraffin film (Bemis Flexible Packaging, Neenah, WI). The container is then positioned in the hutch and a thermocouple (K-type, Omega, Stamford, CT) is inserted through the film of one of the access holes into the liquid agarose. The puncture is resealed with latex sealant.

To ensure the integrity of the agarose for the infusion, the fluid input lines are attached to the needles while the agarose is still liquid.

The perpendicular port of the T-couple is unplugged and any air pockets are removed using a syringe of water tipped with a soft polymer-tipped dispensing needle.

The dye in the input lines and the water in the T-couple are brought into fluid communication before the Luer connector is secured to each needle.

The fluid level in the T-couples in monitored as the agarose cools to ensure it does not drop below the perpendicular port, thereby creating potential for air bubbles or clogging due to dried dye.

The agarose is allowed to sit for at least 6 hours once it has cooled to below the agarose's gelling temperature as recorded by the thermocouple.

Once the agarose has gelled, the occlusion fibers are removed from each needle. The T-couple is topped off with water, and vent lines terminating in stopcocks in the open position are attached. The stopcocks were not attached directly to the needles' Luer connectors in order to keep unnecessary stress of the needles, and to keep handling of the

needles to a minimum. The fluid system is then primed to remove any remaining air, and the stopcocks are closed.

A shadowography technique from similar experiments [19] was modified to capture image date of the infusion from one side and bottom views in addition to the front view. The phantom was placed on an elevated clear-acrylic platform to which light-diffusion panels were attached on two sides. An overhead frame supported the input fluid lines and a third light-diffusing sheet to minimize variations in lighting intensity in each of the three views. A small household light bulb (Energy Smart, 1600 lumen, 2700 K, GE Lighting, Cleveland, OH) was placed directly behind each diffusing panel. Images were captured by a DSLR camera (Canon USA, Rebel T1i, Melville, NY) controlled by a laptop, which captured images at one minute intervals for the duration of each infusion. Front images of the infusion were captured directly by the camera, while side and bottom views were reflected to the camera by angled mirrors. (i.e. all three views were captured simultaneously by the same camera in the same image). Metric scale bars were included in each view.

a) Infusion Parameters

A syringe pump (Harvard Apparatus, Holliston, MA) drove one syringe per active needle in the infusion at a rate of 0.3 ml/min for four hours. The total flow rate into the phantom was 2.1 ml/min. The temperature was monitored, and samples that varied more than 2°C from the 26°C target were discarded.

i. Image Processing and Volume Estimation

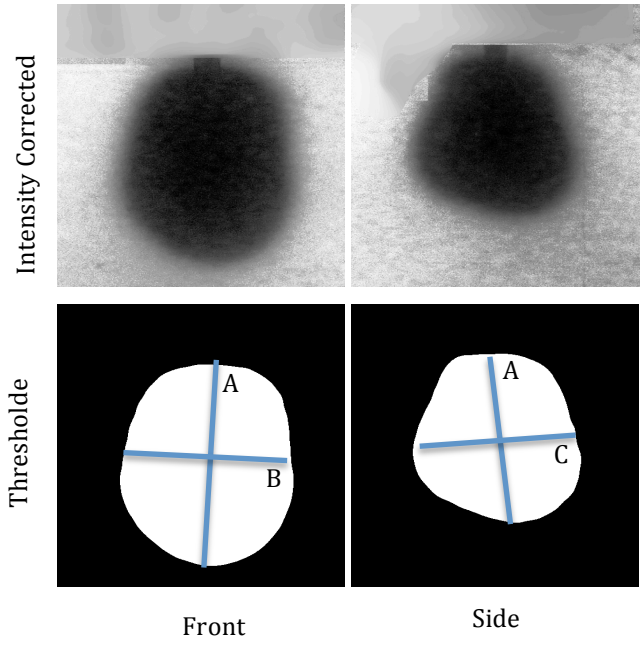

Figure 3-3: Intensity-corrected grey-scale images and corresponding post-processed binary images with representative semi-axes overlaid. Distortion at the top of the intensity images is from manual elimination of irrelevant visual noise.

Final infusion images were processed using MATLAB (The Mathworks, Natick, MA), and ImageJ (NIH, Bethesda, MD). MATLAB extracted the red-intensity channel from the original image, cropped the photo into separate views, normalized the intensity of the front view to that of an external reference file, and normalized the bottom and side view intensities to that of the front view. Intensity normalization was done using the average background intensity of each image as a reference. MATLAB also scaled the pixel sizes of each view using the scale bars included in the frames. Image was used to threshold each image using the built-in IsoData algorithm, and determine the best-fit ellipsoid for each view. The best-fit ellipse has the same area, orientation, and centroid of the original volume's profile. The major and minor axes of each view's ellipsoid were recorded and mapped to the appropriate axes. The major axes of the front and side view were scaled

and averaged to obtain the major axis for the calculated ellipsoid volume. This value and the minor axes from the front and side view were taken to be the semi-axes of a representative 3-dimensional ellipsoid and the approximate volume was calculated using $V_d = (4/3)\pi ABC$, where A, B, and C are the semi-axes of the ellipsoid. The bottom view of the phantom did not yield images easily thresholded using the above algorithm, and so were used as a qualitative comparison for the widths calculated from each of the other views.

b) Preliminary *Ex Vivo* Experiments

The arborizer was implemented during a demonstration of photothermally augmented convection-enhanced delivery in an *ex vivo* canine brain. The arborizing catheter was guided to the target area via an implanted stereotactic plug. Due to anatomical constraints, only three of the seven hollow-core fiberoptic microneedle devices (FMDs) were deployed through the arborizing catheter. 180 uL of Glowing Galbumin were infused into the corpus callosum at a rate of 1 μL/min per FMD (3 μL/min total) over one hour while taking high resolution scans with a 1.5 T superconducting magnet with an 8-channel volume head coil (Philips Integra, Philips Healthcare, Andover, MA). T1-weighted images were collected in 3 planes using a spin echo sequence and 1.5 mm slices. After the infusion, the arborizer and FMDs were left in place, and the head scanned with a CT imager (Toshiba Aquilon, Toshiba, Japan) to confirm the position of the fiberoptic needles. The resulting infusion volume was calculated using the OsiriX® (32-bit v3.3, http://www.osirix-viewer.com) ROI volume tool.

3.3 Results

Final Product of Manufacturing Process

The manufacturing process described above yields a device up to 10 cm long with an outer diameter of less than 2.5 mm. The needles deploy at a 25º angle from the catheter's axis with no motion normal to the needles' axes due to actuation. The ability to manipulate each fiber individually allows the surgeon a high degree of control over the shape of the infusion volume which presently can only be achieved using a multiple-insertion technique. The deployed fiberoptic needles are clearly visible in the brain via CT imaging as seen in Figure 4, and the robust infusion volume is seen in MR images (Figure 6). It is noteworthy that there is negligible reflux of infusate along the primary catheter body. This could be attributed to the sudden geometric change in the device at the needle/catheter junction. The infusate was distributed through a volume of 450.8 μL, and showed preferential distribution along white-matter tracts.

Optical and Mechanical Effects of Helically Deformed Fused Silica Capillary Tubes

The primary advantage of the helical design is that it keeps stress concentrations on the individual needles low by supporting the needle over the entire length within the arborizer. This is in part due to the needle guide constraining only in the radial motion, and aside from negligible friction between the arborizer wall and the needle exterior resisting axial rotation of the needle, the elasticity of the needle allows it to nearly minimize torsional stresses as it is being actuated. The helical configuration allows

multiple needles to bend at relatively large radii about both cross-sectional axes, resulting in the needle exiting the catheter's tip at the desired angle. To achieve this with needles configured radially in the arborizer would require a much smaller radius about a single cross-sectional axis in order to achieve the same deployment configuration. This smaller radius would cause the needle to experience much higher stresses along a shorter length, and therefore more likely to break. When actuated, the smaller radius would cause the needle to exert more pressure against the wall of the arborizer tube, thereby increasing friction and making the needle more difficult for the surgeon to deploy accurately, if at all. Preliminary experiments show the LTSP150375 light guiding capillary tube to have a minimum bend radius of approximately 2.5 mm.

Agarose Infusions

The arborizer infusions showed a mean distribution of 70 mL with a standard deviation of 22.68 mL. The mean V_d/V_i was 139.774 with a standard deviation of 45.01. This distribution ratio is an order of magnitude greater than single-needle infusions under similar conditions [45].

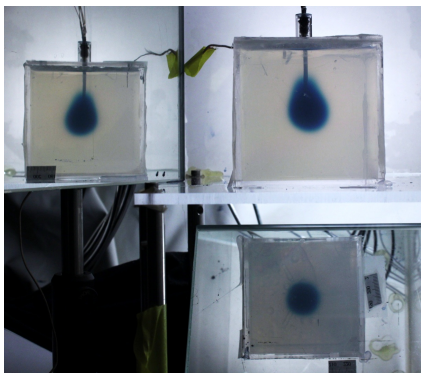

Figure 3-4: 3-view image of post-infusion volume in the shadowgraphy aparatus. The scale bar in the main view lost adhesion during the experiment, however only the first frame was needed to establish the scale of each view, and so it did not effect the data.

Preliminary *ex vivo* and *in vivo* Experiments

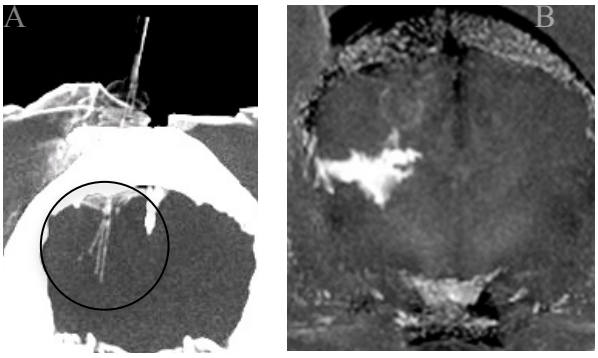

Figure 3-5: a) CT image showing the device deployed in an ex vivo canine brain. b) MR image showing the infused volume.

The CT image in Figure 2a clearly shows the fiberoptic microneedles deployed in the brain. The MR image in Figure 2b shows that after one hour, the infusate had permeated a volume of 0.4415cm^3 with negligible reflux. This gives a ratio of distributed volume to volume infused (V_d/V_i) of 2.45. The infusate showed preferential distribution along white-matter tracts.

The manufacturing process described above yields a device up to 10 cm long with an outer diameter of approximately 2.5 mm. The needles deploy at a 25° angle from the catheter's axis, with no lateral motion due to actuation. The deployed fiberoptic needles are clearly visible in the brain via CT imaging, and the enhanced infusion volume is seen in MR images.

This device was implemented during a demonstration of photothermally augmented convection-enhanced delivery in an *ex vivo* canine brain. It is necessary to be able to visualize deployment of the hollow-core fiberoptic microneedles through the arborizing catheter in the brain as well as the subsequent infusion volume using CT and MR imaging.

3.4 Discussion

As shown above, the mean V_d/V_i ratio for an infusion into agarose with an arborized catheter is an order of magnitude greater than a single needle infusing under similar conditions. This can be attributed to multiple sources distributed through an area approximately 1 cm^2, as opposed to a single CED catheter of dimensions similar to one of the arborizer's deployable needles.

In addition to hollow-core optical fibers, this device can allow multiple solid-core fiber optics, surgical tools such as temperature or pressure sensors, slender capillary tubes, end-effectors, etc., to be guided through a single needle tract to a target area before being deployed. In theory, this minimizes the risk of damaging critical structures due to multiple insertions, or seeding multiple needle tracts with cancer cells or other diseased tissue. Additionally, if the catheter is used with an array of co-delivery FMD's, a LITT treatment of the needle tract can be performed as the catheter is extracted in order to

further reduce the risk of tract seeding, though further research with respect to needle-tract seeding will be required to validate this specific claim.

Further work in tissue phantoms and *in vivo* models will be necessary to compare this arborizing FMD catheter design to conventional CED catheters using such metrics as reflux, allowable infusion rates, and distribution volumes. However, initial results indicate that the arborizing catheter can treat the same or greater volume than a standard non-arborizing catheter using a slower per-needle flow rate, thus further decreasing reflux, and/or decreasing required infusion time compared to a standard CED catheter depending on the specific requirements of a given situation. Since each needle within the catheter can be manipulated independently, custom infusion geometries can be easily created, and when implemented with co-delivery FMDs, further manipulated by varying the optical power output of each needle.

3.5 Conclusion

Preliminary *In Vivo* and *Ex Vivo*

These results demonstrate that the arborizing catheter described herein can infuse very large volumes comparatively short periods within an accepted brain tissue phantom. Additionally, our preliminary work shows that this design can be deployed intracranialy and infuse fluid. Further work in *in vivo* models will be necessary to compare this arborizing FMD catheter design to conventional CED catheters, however the results of this initial trial in agarose phantoms shows that the arborizing catheter concept has potential.

Chapter 4: *In Vivo* Co-Delivery of Single Walled Carbon Nano-horns and Laser Light to Treat Human Transitional Cell Carcinoma of the Urinary Bladder in a Rodent Model

4.1 Introduction

Bladder cancer is the fourth most prevalent noncutaneous malignancy in the United States, with approximately 70,980 new cases in 2009 alone [22]. Approximately 30% of new diagnoses are already at an advanced clinical stage (stage 2-3), meaning the tumors have already penetrated into the muscular and serosal layers of the bladder, and metastasized to surrounding organs [23].

Currently, the primary treatment for superficial bladder cancer is transurethral cystoscopic resection and fulguration [37] is successful in arresting tumor progression in approximately 80% of cases of superficial bladder cancer. Approximately 90% of bladder cancers are transitional cell carcinomas (TCCs)[23]. At the time of diagnosis, approximately 30% of bladder tumors are at an advanced clinical stage, with penetration into or through the bladder wall (AJCC T2-3). Once the cancer has progressed to these stages, the typical survival rate drops to 30-50%, even with radical, multimodality treatment [23]. Treatment of such advanced stages of bladder cancer frequently results in sexual dysfunction, electrolyte imbalances, bone loss, and deterioration of the kidney. Following complete cystectomy, the preferred treatment of advanced bladder cancer, an alternative urine excretory system is necessary; this may be constructed from part of the intestines or the patient may require an external pouch or ostomy device system [37], [38].

Laser-induced thermotherapy (LITT), in which an optical probe is inserted into the bladder and thermally ablates superficial tumors, has been successfully employed and shown to yield therapeutic results comparable to transurethral resection, but with fewer complications and better patient recovery[39]. Systemically-administered and intravesicular photosensitizers or photoabsorbers (Photodynamic Therapy, or PDT) have been used to enhance the selectivity and efficiency of LITT[40]. However, these therapies are sufficient for little more than treating superficial lesions because wavelengths typically used only penetrate on the order of 1mm. For tumors penetrating into and past the underlying muscle, this often results in poorly defined lesion boundaries and a high likelihood of tumor re-growth, recurrence, and necrosis of the bladder wall. LITT and PDT, though showing potential, are also limited by the ability to administer photoabsorbers in sufficient amounts to effect tumor cells or to selectively distribute photosensitizing molecules with a defined distribution in the appropriate tumor region.

Recognizing the limitations of LITT and PDT, we have invented a fiberoptic microneedle device (FMD) that allows significantly enhanced laser light penetration to desired target tissue depths by using near-infrared (NIR) laser light and selective amplification of thermal dose through local introduction of exogenous photo absorbers such as nanoparticles or therapeutic agents.

In this study, the exogenous chromophore we selected are single-walled carbon nanohorns (SWNH). SWNHs have been used with 67 nm laser irradiation to reduce the size of mouse tumors [41], and our group has shown the ability to destroy kidney tumor cells when laser irradiation at 1064 nm was used in combination with SWNHs. Due to selective absorption of optical radiation by the SWNHs in the target tissue, the optical

dose can be more precisely controlled, reducing unwanted collateral tissue damage and associated pain. In other words, the optical dose could be of a low enough power level so that the light alone would not damage the tissue, but SWNHs infused in the target area would absorb enough light to generate clinically relevant levels of heat.

The objective of this study is to determine the therapeutic efficacy of the FMD for treating bladder cancers located within the muscular and serosal layers based on nanoparticle-enhanced photothermal treatment using a well-accepted rodent model of invasive transitional cell carcinoma [42].

4.2 Methods

AY27 Cell Culture

The transplantable AY27 urothelial carcinoma cell line (Department of Urology, Medical College of Ohio, Toledo, OH). This cell line was originally derived from exposure of Fisher 344 rats to the chemical carcinogen N-[4-(5-nitro-2-furyl)-2-thiazolyl] formamide (FANFT). On receipt, cells were cultured in RPMI Medium 1640 (Invitrogen; Grand Island, NY) supplemented with 10% fetal bovine serum (FBS, Sigma Aldrich; St. Louis, MO), 1% penicillin and streptomycin (Sigma Aldrich), and were maintained in a humidified atmosphere at 37^{o} C with 5% CO2 and 95% air. Cells were passaged every four days prior to reaching 80% confluency. Passage numbers 37–42 were used for all experiments.

Animal Husbandry

Young, female F344 rats were purchased from a commercial vendor (Charles River Laboratory Animals, Wilmington, MA). After receipt and seven-day quarantine period,

rats were housed singly in barrier-maintained polypropylene cages, supplied with standard laboratory rodent chow (Teklad 2918 Irradiated Rodent Chow, Teklad Diets, Harlan Laboratories, Madison, WI), and allowed public water *ad libitum* through an automatic watering system. According to protocol, rats were handled and observed twice weekly for health and socialization.

Tumor Induction and Characterization

AY27 cells (above) were harvested at confluence and suspended in RPMI-1640 medium at a density of 1 x 10^6 cells per ml. Rats were gently restrained and a 1 mL. injection (1 x 10^6 cells) was given in either the lateral aspect of the left hind leg or in the mammary fat pad of the left inguinal region. These sites were chosen for studies to permit ready observation of tumor growth and for access for treatment with the FMD device. Tumors were periodically induced in groups of 5-10 rats for study.

SWNH Solution Preparation

Weighed SWNH powder was rinsed into a filtration system located within a sterile hood onto a 0.1 μm PTFE filter. SWNHs were washed with a volume of 10-15 mL of ethanol followed by 2-3 additional washes of sterile water. Following washing, the filter was introduced to a solution containing sterile water and 1%wt pluronic (sterile) to yield the desired concentrations for experiments. SWNHs were transferred off of the filter through sonication for 1-2 minutes, after which the filter was removed from solution. The solution was vortexed for 5 minutes to ensure that SWNHs were well mixed in the pluronic

solution. Before use, solution was transferred to a sterile 1 mL vial with a rubber septum cap.

FMD Fabrication

The FMDs (Figure 1) were constructed by inserting commercially available optical fiber (FIP100110125, Polymicro Technologies, Downers Grove, IL) through a fluid T-couple connected to a 14G catheter with a fused silica capillary tube bevel polished at the tip. The distal end of the T-couple was sealed with epoxy to prevent infusate leakage and to hold the fiber in place. The other two ports were left unmodified to allow fluid flow. The optical fiber was cleaved so that it terminated ~1mm behind the bevel of the tip in order to prevent damage upon insertion into tissue. The tip of the device was made of fused silica to prevent it from absorbing 1064 nm laser light and burning the surrounding tissue as a stainless steel needle would have. The goal of this device is not to ablate tissue using a point source, but to allow light to penetrate a volume and selectively heat infused nanoparticles.

A 30G T-type microthermocouple is attached so that the probe is parallel to the capillary tube, and the tip terminates ~0.5mm behind the cleaved fiber tip with sufficient insulation/spacing so as not to be heated by the laser directly.

Once fabricated, FMDs were assessed for ability to deliver both fluid through the cannulus, and photon energy via the optical fiber nested within. The robustness and repeatability of fabrication was assessed by repeated bench-top testing of energy output and for continuity of fluid delivery (absence of leaks).

Devices that were suitable were then tested in normal (non-tumor bearing) animals as a device control. For this testing, rats were anesthetized and prepared for aseptic surgery (see below). The FMD was inserted through a small incision in the skin on the lateral aspect of the left hind leg. SWNH solution and laser energy were then delivered (as described below, for tumor-bearing animals). Muscle and subcutaneous tissue were then heated to 60^{o}C (as indicated by the device thermocouple). Animals were recovered from anesthesia and observed for signs of thermal damage to treated tissues for periods up to 7 days.

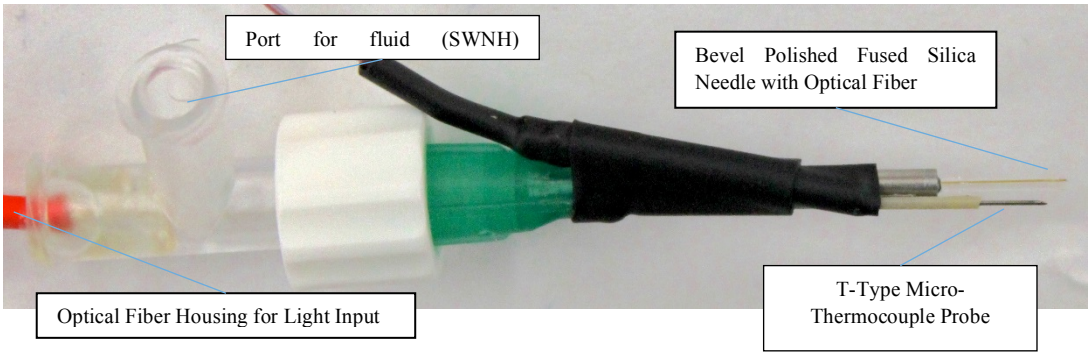

Figure 4-1: Fiberoptic Microneedle Device (FMD) used for treatment of rats with implanted urothelial cell carcinomas.

Concentration and Power Range Finding

Non-sterile solutions of SWNH were prepared in D.I. water and 1%wt pluronic at concentrations of 0 (control), 0.17 mg/mL, and 0.255 mg/mL. Food-grade porkbelly (~24-48 hours post-slaughter, refrigerated) was trimmed of muscle, leaving only the skin and a layer of subcutaneous fat. The skin was laid epidermis down on a custom isothermal hotplate and covered in a layer of isotonic saline-soaked paper towels to prevent drying. A layer of aluminum foil was also added to maintain a consistent thermal gradient through the skin. Temperature was maintained at 36+/-1 °C.

For treatment, a small area was uncovered and the device inserted ~3 mm laterally and ~1mm below the surface of the subcutaneous fat. 50-100 μL of SWNH solution was injected, and the device withdrawn ~1 mm to ensure that the solution bolus was in the path of the laser. NIR laser irradiation was applied at 500 or 1000 mW for 3 minutes and the treated area was allowed to cool for three minutes. Temperature data was recorded through the full cycle. Each treatment was tested at N=5.

Tumor Treatment with FMD and SWNH

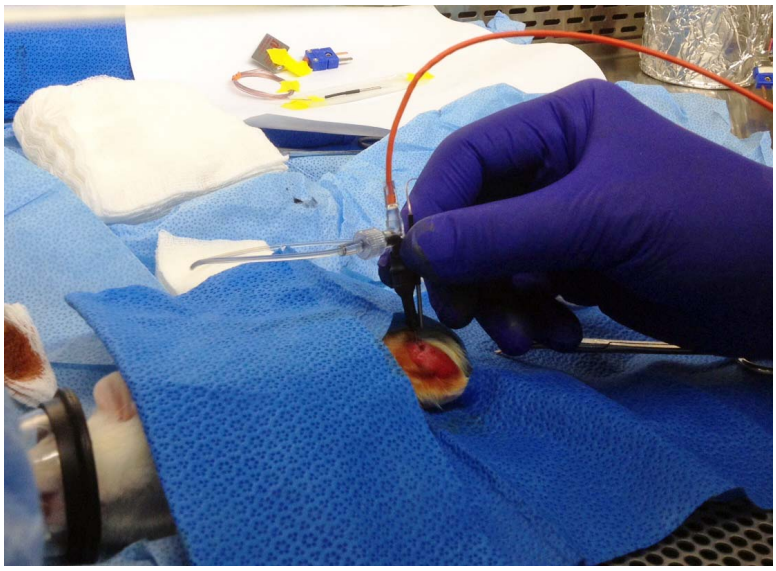

Figure 4-2: Placement of FMD in urothelial cell carcinoma prior to treatment.

When tumors had reached a sufficient size (5-10 mm^3) for study, rats were anesthetized with inhaled isoflurane gas/oxygen. Tumors were measured and the hair over tumors on the lateral aspect of the skin of the left hind leg was shaved and prepared for aseptic surgery. A 20G needle was used to create a small hole in the skin that was then enlarged to 3 mm length for insertion of the FMD treatment device. Once the device was positioned in the tumor and operation of the thermocouple verified, a 0.255 mg/mL solution of SWNH as injected (See Figure 4-2).

Following administration of the SWNH, photon energy was applied (a laser power of 1 W was used; the laser was a 1064 nm continuous wave Nd:YAG source). The internal temperature of the tumor at the site of the device was measured, using a thermocouple co-joined to the tip of the FMD. Based on previous experiments, tumors were energized until a temperature of 60^{o}C was achieved (generally within two minutes). The laser was then

turned off and the device removed. The animal was allowed to recover from the effects of anesthesia, and then observed daily for effects of treatment or the presence of undesirable or unanticipated side effects. Any rat displaying discomfort was humanely sacrificed. Seven to 14 days later, rats that had been treated were deeply anesthetized and then humanely sacrificed. Treatment sites were photographed then dissected and placed in 10% buffered formalin for fixation and histologic examination. Histologic sections were prepared, stained with hematoxylin-eosin stain, and evaluated by a qualified pathologist.

4.3 Results

Range Finding

Pluronic at 500 mW and 0.17 mg/mL at 500 mW were nearly identical, and pluronic at 1000 mW showed a slight increase above the lower powered runs (Table 1/Figure 3). However, 0.17 mg/mL at 1000 mw and 0.255 mg/mL at 500 mW both showed similar significant temperature increases, suggesting that the optimal concentration/power combination lies between the two.

Table 4-1: Mean Maximum Temperatures

NIR Laser Power	Pluronic Only	0.17 mg/mL	0.255 mg/mL
1000 mW	59.79 ± 33.57°C	101.85 ± 30.58°C	110.18 ± 13.04°C
500 mW	59.12 ± 8.6°C	59.54 ± 5.15°C	93.77 ± 18.89°C

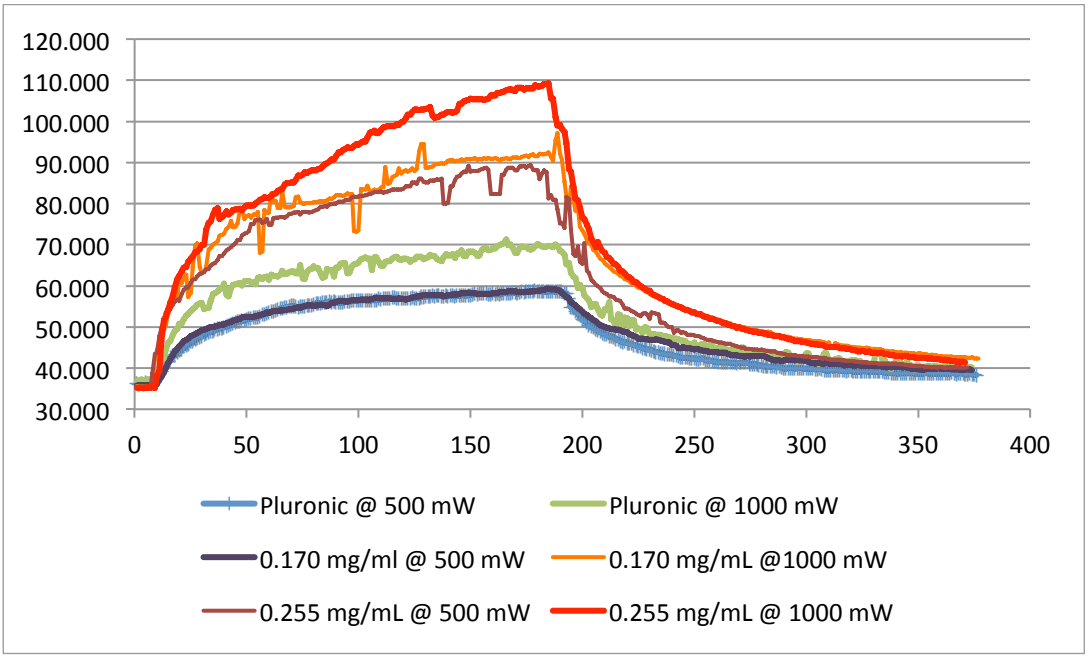

Figure 4-3: Heating and Cooling Curves

0.255 mg/mL at 500 mW seemed to be the most effective without excessive burning, while 1000 mW at the same concentration charred the tissue every time (Figure 4-4).

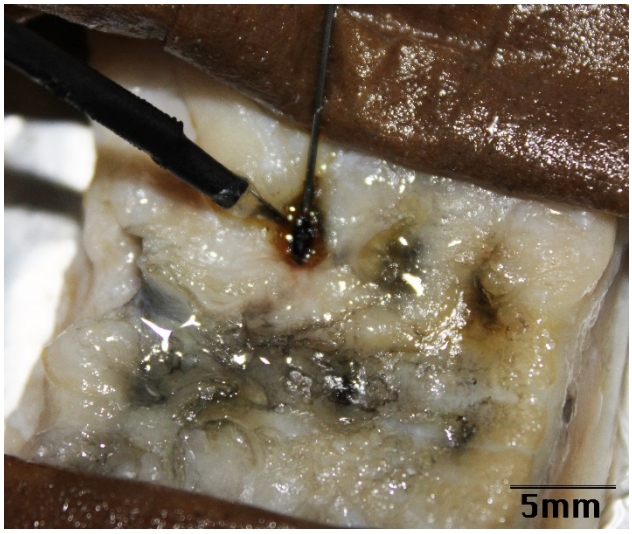

Figure 4-4: Charring due to 100 mW 0.255 mg/mL treatment (upper row). Note the row of pock marks without charring from the 500 mW 0.255 mg/mL treatment (lower row).

Significant heating was achieved with 0.17 mg/mL at 1000 mW. Similar heating was achieved with 0.255 mg/mL at 500 mW, suggestion that the higher concentration captured a higher percentage of the photons emitted thus generating roughly the same amount of heat with less over-penetration of light, thus protecting structures and tissues beyond the treatment area.

Device Control Testing

Three non-tumor bearing control rats were treated with the FMD. The goal of this treatment was assessment of device placement and discernment of effects of heating on normal tissue. Thermal necrosis of tissue was achieved at the site of treatment in all three rats. We noted that it took a considerable period of time (up to 5 minutes) to achieve the thermal temperature goal (60^{o}C); in two rats the rate of rise of temperature was very slow; we felt this reflected dissipation of thermal energy from physiologic vasodilation around the treatment site. This is quite relevant. As the FMD evolves into a clinical treatment device, it will be important to position it to allow normal tissues to be 'avoided' by treatment and to also exploit normal tissue physiologic (protective) responses in creating discrete zones of treatment.

Tumor Induction and Characterization

Tumor growth was characterized by a long latency between injection of the AY27 cells and development of palpable (>3mm) subcutaneous tumors. In most rats, this period of latency was >6 weeks; typically ~8-9 weeks. Once established and past the period of

latency, tumors grew rapidly over a 1-2 week period. The rate with which tumors were induced was approximately 60%. The site of tumor induction influenced tumor growth. Tumor suspensions administered in the lateral aspect of the leg were more likely to produce tumors than suspensions administered in the mammary fat pad.

Figure 4-5: (Left) Post-mortem specimen of a typical small subcutaneous urothelial cell carcinoma in the left hind limb, lateral aspect. Following injection of 1 x 10^6 tumor cells, these masses appeared within 6-8 weeks. The cystic nature of the mass is readily appreciated from the photograph. There was some variation in the size and shape of masses at 6-8 weeks (compare with photo on right). Photo by Dr. John L. Robertson, 2014, used with permission.

Tumors typically appeared as elongate, subcutaneous palpable masses on the lateral aspect of the leg. Tumors were non-painful and were firmly anchored to the tissue underneath them, thus not freely movable. Uneven consistency and rapid enlargement suggested the formation of cystic cavities; this was confirmed on gross post-mortem examination (Figure 4-5, below). Tumors were histologically examined and could be readily classified as moderately differentiated cystic transitional cell carcinomas (Figure 4-6). Some tumors developed pseudoglandular morphology with anastomosing ribbon-like cell aggregates. Others were present as pleomorphic solid carcinomas. All tumors had interspersed areas of necrosis, where cell growth had exceeded vascular support.

Tumor cells varied in size and shape, with a predominance of indented polygonal to rounded shapes and marked variation in cell size. Cell nuclei varied from rounded to ovoid and indented/molded. Mitotic figures were considered moderately common (>10 HPF).

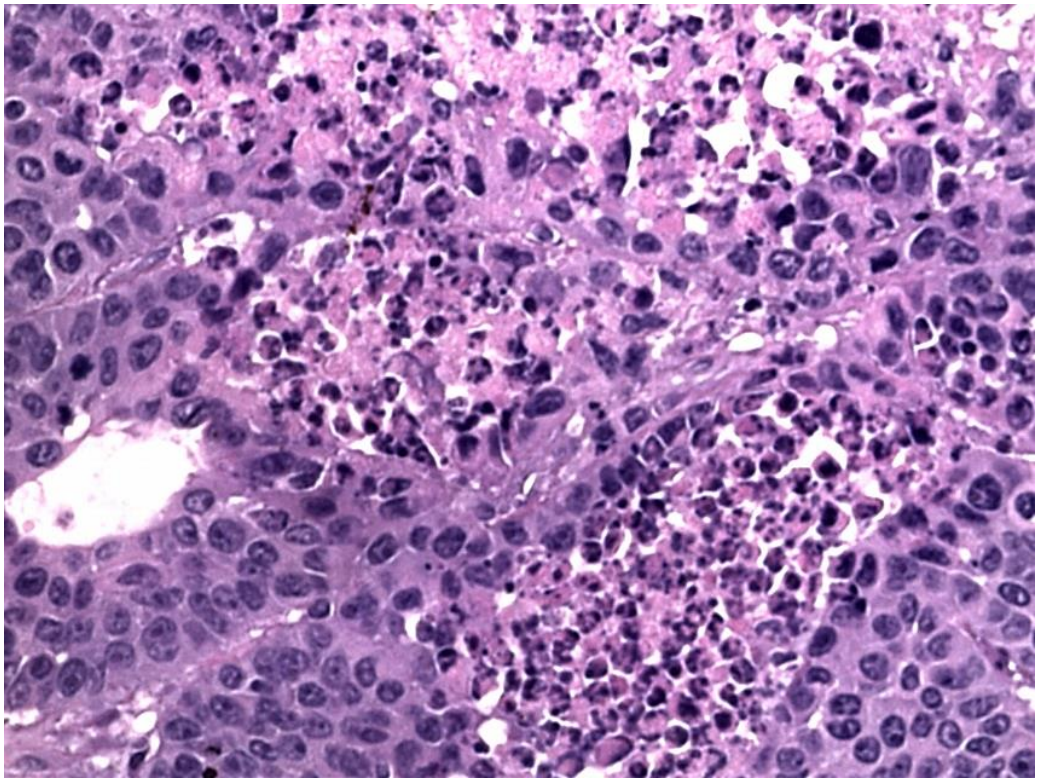

Figure 4-6: Histologic image of urothelial cell tumor. Tumor cells formed sheets and pseudoglandular aggregate with cystically dilated lumina. There is a brisk mitotic rate and moderate cellular pleomorphism. Areas of necrosis are evident. HE stain, magnification 20x. Photo by Dr. John L. Robertson, 2014, used with permission.

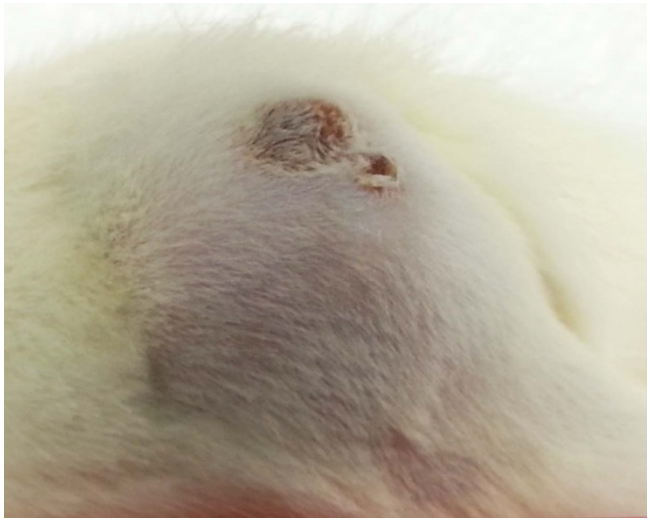

Figure 4-7: Focus of ulceration and drainage on the skin of a rat with urothelial cell carcinoma that was treated by administration of SWNH, and photon energy sufficient to heat a portion of the tumor mass to 60°C. Photo by Dr. John L. Robertson, 2014, used with permission.

Tumor Treatment

Treatment of tumors with SWNH, followed by photon-induced heating of the nanohorns, resulted in thermal necrosis of tumor cells. As noted previously, the period of time needed to reach 60^{o}C within the tumor varied among animals and tumors. Those tumors with large cystic spaces immediately adjacent to the point of treatment tended to heat more slowly (several minutes). Grossly, portions of the tumor and overlying skin (See Figure 4-7) developed ulceration, liquefactive necrosis, and drainage.

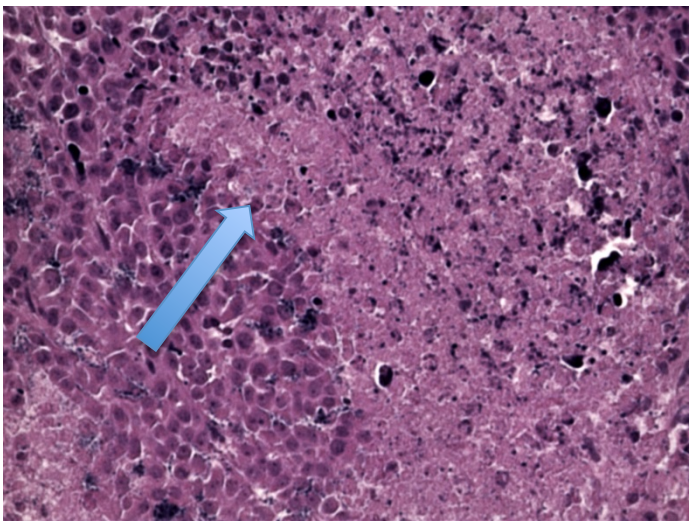

Figure 4-8: Histologic image of thermally-damaged tumor tissue. A sharp line of demarcation (arrow) separates viable and necrotic tumor tissue. HE stain, magnification 20x. Photo by Dr. John L. Robertson, 2014, used with permission.

Histological assessment of areas of FMD treatment correlated well with gross morphologic appearance. There was both coagulative and liquefactive necrosis of tumor tissue seen acutely (within 24-48 hours of treatment) (Figure 4-8). Foci of tumor necrosis showed rather sharp (1-2 mm) delineation from areas of viable tumor (not treated) and normal tissue. In some rats and tumors, it was somewhat difficult to determine the shape of areas of treatment/necrosis, as devitalized tumor appeared as anastomosing fingerlets diverging from the site of treatment. In some tumors, there were also areas of focal necrosis not associated with treatment; these were distant from the site of device placement and it was unlikely that they resulted from direct SWNH-mediated heating. However, it is possible that FMD treatment may have damaged blood vessels coursing within or adjacent to treatment site and possibly infracting distant tissues. It is also possible that these foci of tumor necrosis distant from the site of FMD treatment were areas in which rapid growth of the urothelial carcinoma or compression from formation

of cystic cavities compressed vasculature and/or tumor tissue, resulting in tumor tissue necrosis.

At 7 days after FMD treatment, fibrovascular proliferation and resolving acute inflammation was seen in tumor-bearing rats. These areas were considered typical of the reaction that would accompany resolution of thermal injury.

In three tumor-bearing rats that received FMD treatment, progressive paresis and paralysis of the treated leg was noted within 24 hours of tumor therapy. The explanation for this progressive paresis/paralysis was thermal damage to the nerves serving the limb. There was flaccidity of both flexor and extensor responsiveness and lack of response to stimulation of the bottom of the foot or to the toes on the affected limb. In each case, these rats had large, cystic tumors and the period of time needed to raise internal tumor temperature to 60°C was prolonged (>5 minutes). According to protocol, these rats were sacrificed for humane considerations. With subsequent rats, significant efforts were made to avoid FMD placement and heating near nerve structures. This was successful and treated rats did not develop paresis/paralysis in the 7-day post-treatment observation period.

4.4 Discussion and Conclusion

We were able to demonstrate proof-of-concept for FMD-mediated tumor treatment in rats with subcutaneously-implanted urothelial carcinomas. Previous studies [43], [44] determined that heating of tumor cells in both two-dimensional and three-dimensional tissue cultures, relatively rapidly, to temperatures >45^{o}C, would kill them. We chose a

target temperature of approximately 60^{o}C for *in vivo* therapy. There were several reasons for our choices and treatment parameters:

- Although we were fairly certain that most, if not all, tumor cells would be killed at 45^{o}C, we were not certain we would uniformly achieve this 'minimum killing temperature' except in close proximity (within 1 mm) to the tip of the FMD,
- We were not certain if the shape and composition of implanted tumors would either propagate or insulate thermal events at the FMD tip,
- We were not certain if normal and tumor vasculature would dissipate thermal energy, resulting in a sub-therapeutic (<45^{o}C) temperature within the area of treatment,
- We were not certain if heating would be rapid or slow, or what the amount of variation from tumor to tumor would be, based on tumor life cycle, infiltration into surrounding musculature, or spontaneous necrotic voids,
- Thus, we opted for a higher initial treatment temperature.

We believe we have demonstrated the feasibility of using the FMD for treatment of urothelial carcinoma, using an animal model of this disease. We successfully fabricated multiple prototypes, with each successive fabrication growing in functionality and robustness. It is worth noting that the rangefinding temperatures were obtained using an earlier generation of the design which did not incorporate an affixed thermocouple. The thermocouple was placed in the treatment area by hand resulting in variations in distance from the tip of the device, thus accounting for the large standard deviations in the treatment temperatures. Our final design incorporates a unique co-couple device to administer therapeutics (in this case, SWNH) and tunable energy. Experience with

device prototypes in tissue cultures of cancer cells, biological phantoms (collagen and alginate phantoms), freshly-procured tissue specimens (porcine bladders and skin), and *in vivo* modeling in pigs allowed engineering evolution and fabrication of a therapeutically useful medical device. We were able to adapt this device to use with a standard human cystoscope and follow a therapeutic protocol (in pigs) that would be suitable for translation to humans. We successful used a functional equivalent of our prototype in tumor-bearing rats and successfully induced tumor cell death in our rat model of human transitional cell carcinoma. We noted that lesions created by the device and treatment paradigm could be anticipated to spare normal tissue, based on the relatively sharp demarcation between treated and non-treated areas. Likewise, we noted that normal tissue might be protected from severe, acute thermal injury by heat dissipation from the treatment site by intact 'patient' vascular beds.

In conclusion, we are encouraged to continue development of this novel medical device platform that may be especially useful in the treatment of bladder cancer, lung cancer, and solid tumors accessible to the placement of this relatively minute device with medical instrumentation (cystoscopes, laparoscopes, and bronchoscopes).

References

[1] R. Nishikawa, "Standard therapy for glioblastoma--a review of where we are.," *Neurol. Med. Chir. (Tokyo)*, vol. 50, no. 9, pp. 713–719, 2010.

[2] R. Stupp, M. E. Hegi, W. P. Mason, M. J. van den Bent, M. J. B. Taphoorn, R. C. Janzer, S. K. Ludwin, A. Allgeier, B. Fisher, K. Belanger, P. Hau, A. A. Brandes, J. Gijtenbeek, C. Marosi, C. J. Vecht, K. Mokhtari, P. Wesseling, S. Villa, E. Eisenhauer, T. Gorlia, M. Weller, D. Lacombe, J. G. Cairncross, R.-O. Mirimanoff, European Organisation for Research and Treatment of Cancer Brain Tumour and Radiation Oncology Groups, National Cancer Institute of Canada Clinical Trials Group, "Effects of radiotherapy with concomitant and adjuvant temozolomide versus radiotherapy alone on survival in glioblastoma in a randomised phase III study: 5-year analysis of the EORTC-NCIC trial.," *Lancet Oncol.*, vol. 10, no. 5, pp. 459–466, May 2009.

[3] M. D. Walker, S. B. Green, D. P. Byar, E. Alexander, U. Batzdorf, W. H. Brooks, W. E. Hunt, C. S. MacCarty, M. S. Mahaley, J. Mealey, G. Owens, J. Ransohoff, J. T. Robertson, W. R. Shapiro, K. R. Smith, C. B. Wilson, and T. A. Strike, "Randomized comparisons of radiotherapy and nitrosoureas for the treatment of malignant glioma after surgery.," *N. Engl. J. Med.*, vol. 303, no. 23, pp. 1323–1329, Dec. 1980.

[4] D. W. Laske, R. J. Youle, and E. H. Oldfield, "Tumor regression with regional distribution of the targeted toxin TF-CRM107 in patients with malignant brain tumors," *Nat. Med.*, vol. 3, no. 12, pp. 1362–1368, Dec. 1997.

[5] R. H. Bobo, D. W. Laske, A. Akbasak, P. F. Morrison, R. L. Dedrick, and E. H. Oldfield, "Convection-enhanced delivery of macromolecules in the brain," *Proceedings of the ...*, pp. 1–5, Jan. 2013.

[6] A. A. Kanner, "Convection-Enhanced Delivery," *Current Clinical Oncology*, pp. 303–314, 2007.

[7] W. A. Vandergrift, S. J. Patel, J. S. Nicholas, and A. K. Varma, "Convection-enhanced delivery of immunotoxins and radioisotopes for treatment of malignant gliomas.," *Neurosurg Focus*, vol. 20, no. 4, p. E13, 2006.

[8] J. H. Sampson, G. Archer, C. Pedain, E. Wembacher-Schröder, M. Westphal, S. Kunwar, M. A. Vogelbaum, A. Coan, J. E. Herndon II, R. Raghavan, M. L. Brady, D. A. Reardon, A. H. Friedman, H. S. Friedman, M. I. Rodríguez-Ponce, S. M. Chang, S. Mittermeyer, D. Croteau, and R. K. Puri, "Poor drug distribution as a possible explanation for the results of the PRECISE trial," *Journal of Neurosurgery*, vol. 113, no. 2, pp. 301–309, Aug. 2010.

[9] M. Bettag, F. Ulrich, R. Schober, and G. Fürst, "Stereotactic laser therapy in cerebral gliomas," *Advances in Stereotactic ...*, 1991.

[10] A. Carpentier, J. Itzcovitz, D. Payen, B. George, R. J. McNichols, A. Gowda, R. J. Stafford, J.-P. Guichard, D. Reizine, S. Delaloge, and E. Vicaut, "REAL-TIME MAGNETIC RESONANCE-GUIDED LASER THERMAL THERAPY FOR FOCAL METASTATIC BRAIN TUMORS," *Neurosurgery*, vol. 63, pp. ONS21–ONS29, Jul. 2008.

[11] A. Carpentier, D. Chauvet, V. Reina, K. Beccaria, D. Leclerq, R. J. McNichols,

A. Gowda, P. Cornu, and J.-Y. Delattre, “MR-guided laser-induced thermal therapy (LITT) for recurrent glioblastomas.,” *Lasers Surg. Med.*, vol. 44, no. 5, pp. 361–368, Jul. 2012.

[12] H.-J. Schwarzmaier, I. V. Yaroslavsky, A. N. Yaroslavsky, V. Fiedler, F. Ulrich, and T. Kahn, “Treatment planning for MRI-guided laser-induced interstitial thermotherapy of brain tumors—The role of blood perfusion,” *J. Magn. Reson. Imaging*, vol. 8, no. 1, pp. 121–127, 1998.

[13] R. J. Stafford, D. Fuentes, A. A. Elliott, J. S. Weinberg, and K. Ahrar, “Laser-induced thermal therapy for tumor ablation.,” *Crit Rev Biomed Eng*, vol. 38, no. 1, pp. 79–100, 2010.

[14] B. Schwabe, T. Kahn, T. Harth, F. Ulrich, and H.-J. Schwarzmaier, “Laser-induced thermal lesions in the human brain: short-and long-term appearance on MRI,” *Journal of computer assisted tomography*, vol. 21, no. 5, pp. 818–825, 1997.

[15] A. H. Saad and G. M. Hahn, “Ultrasound-enhanced effects of adriamycin against murine tumors.,” *Ultrasound Med Biol*, vol. 18, no. 8, pp. 715–723, 1992.

[16] A. N. Yaroslavsky, P. C. Schulze, I. V. Yaroslavsky, R. Schober, F. Ulrich, and H. J. Schwarzmaier, “Optical properties of selected native and coagulated human brain tissues in vitro in the visible and near infrared spectral range.,” *Phys Med Biol*, vol. 47, no. 12, pp. 2059–2073, Jun. 2002.

[17] C. P. Palmer, W. R. Laws, and M. D. DeGrandpre, “Characterization of long pathlength capillary waveguides for evanescent fluorescence sensing applications,” *Sensors and Actuators B …*, 2008.

[18] B. K. Keller and M. D. DeGrandpre, “SPIE | Proceeding | Characterization of long pathlength capillary waveguides for evanescent chemical sensing applications,” *Optics*, 2004.

[19] R. L. Hood, J. H. Rossmeisl, R. T. Andriani, A. R. Wilkinson, J. L. Robertson, and C. G. Rylander, “Intracranial hyperthermia through local photothermal heating with a fiberoptic microneedle device.,” *Lasers Surg. Med.*, vol. 45, no. 3, pp. 167–174, Mar. 2013.

[20] Raghu Raghavan, Martin L Brady, María Inmaculada Rodríguez-Ponce, Andreas Hartlep, Christoph Pedain, John H Sampson, “Convection-enhanced delivery of therapeutics for brain disease, and its optimization,” *http://dx.doi.org/10.3171/foc.2006.20.4.7*, 2006.

[21] S. Puccini, N.-K. Bär, M. Bublat, T. Kahn, and H. Busse, “Simulations of thermal tissue coagulation and their value for the planning and monitoring of laser-induced interstitial thermotherapy (LITT).,” *Magn. Reson. Med.*, vol. 49, no. 2, pp. 351–362, Feb. 2003.

[22] “What are the key statistics about bladder cancer?,” *http://www.cancer.org/cancer/bladdercancer/detailedguide/bladder-cancer-key-statistics*, 13-May-2009. [Online]. Available: http://www.cancer.org/docroot/cri/content/cri_2_4_1x_what_are_the_key_statistics_for_bladder_cancer_44.asp. [Accessed: 14-Feb-2010].

[23] M. L. Quek, J. P. Stein, P. W. Nichols, J. Cai, G. Miranda, S. Groshen, S. Daneshmand, E. C. SKINNER, and D. G. SKINNER, “Prognostic significance of lymphovascular invasion of bladder cancer treated with radical cystectomy.,”

The Journal of urology, vol. 174, no. 1, pp. 103–106, Jul. 2005.
[24] D. B. Ingham and I. Pop, *Transport Phenomena in Porous Media*. Elsevier, 1998.
[25] F. A. L. Dullien, *Porous Media*. 1992.
[26] X. Chen, G. W. Astary, T. H. Mareci, and M. Sarntinoranont, "In Vivo Contrast-Enhanced MR Imaging of Direct Infusion into Rat Peripheral Nerves," *Ann Biomed Eng*, vol. 39, no. 11, pp. 2823–2834, Aug. 2011.
[27] Z.-J. Chen, G. T. Gillies, W. C. Broaddus, S. S. Prabhu, H. Fillmore, R. M. Mitchell, F. D. Corwin, and P. P. Fatouros, "A realistic brain tissue phantom for intraparenchymal infusion studies.," *Journal of Neurosurgery*, vol. 101, no. 2, pp. 314–322, Aug. 2004.
[28] P. M. Adler, *Porous Media*. Butterworth-Heinemann, 1992.
[29] K. Roth, *Soil Physics*, no. Daily. Heidelburg, Germany.
[30] F. P. Incropera, D. P. DeWitt, T. L. Bergman, and A. S. Lavine, *Fundamentals of Heat and Mass Transfer 5th Edition with IHT2.0/FEHT with Users Guides*. Wiley, 2001.
[31] C. Slywotzky and M. Maya, "Needle tract seeding of transitional cell carcinoma following fine-needle aspiration of a renal mass," *Abdom Imaging*, vol. 19, no. 2, pp. 174–176, Mar. 1994.
[32] B. J. Glasgow, H. H. Brown, A. M. Zargoza, and R. Y. Foos, *Quantitation of tumor seeding from fine needle aspiration of ocular melanomas*. Am J Ophthalmol, 1988.
[33] K. J. Denton, D. W. Cotton, R. A. Nakielny, and J. R. Goepel, "Secondary tumour deposits in needle biopsy tracks: an underestimated risk?," *Journal of Clinical Pathology*, vol. 43, no. 1, p. 83, Jan. 1990.
[34] D. H. S. Schwartz and D. M. Spengler, "Needle tract recurrences after closed biopsy for sarcoma: Three cases and review of the literature," *Annals of Surgical Oncology*, vol. 4, no. 3, pp. 228–236, Apr. 1997.
[35] P. S. Feldman and M. J. Kaplan, "Fine-needle aspiration in squamous cell carcinoma of the head and neck," *Archives of ...*, 1983.
[36] M. T. Krauze, R. Saito, C. Noble, M. Tamas, J. Bringas, J. W. Park, M. S. Berger, and K. Bankiewicz, "Reflux-free cannula for convection-enhanced high-speed delivery of therapeutic agents.," *Journal of Neurosurgery*, vol. 103, no. 5, pp. 923–929, Nov. 2005.
[37] "Bladder Cancer Treatment," *cancer.gov*. [Online]. Available: http://www.cancer.gov/cancertopics/pdq/treatment/bladder/Patient/page4. [Accessed: 2010].
[38] J. B. Thrasher and E. D. Crawford, "Current management of invasive and metastatic transitional cell carcinoma of the bladder.," *The Journal of urology*, vol. 149, no. 5, pp. 957–972, May 1993.
[39] G. B. Muraro, R. Grifoni, and L. Spazzafumo, "Endoscopic therapy of superficial bladder cancer in high-risk patients: Holmium laser versus transurethral resection," *Surgical technology ...*, 2005.
[40] R. Anderson and J. Parrish, "Selective photothermolysis: precise microsurgery by selective absorption of pulsed radiation," *Science*, vol. 220, no. 4596, p. 524, 1983.

[41] X. Fan, J. Tan, G. Zhang, and F. Zhang, “Isolation of carbon nanohorn assemblies and their potential for intracellular delivery,” *Nanotechnology*, 2007.

[42] S. Yamaguchi, T. Kobayashi, Y. Saito, and K. Chiba, “Efficient Nd: YAG laser end pumped by a high-power multistripe laser-diode bar with multiprism array coupling,” *Applied optics*, 1996.

[43] C. Rylander and M. N. Rylander, “Spatial Measurement of Viability in Tissue Phantoms and Ex Vivo Bladder Tissue in Response to Photothermal Therapy and Single Walled Carbon Nanohorns,” *ASME 2012 ...*, 2012.

[44] A. Rodgers, M. A. Kosoglu, and M. N. Rylander, “Spatially controlled photothermal heating of bladder tissue through single-walled carbon nanohorns delivered with a fiberoptic microneedle device,” *Lasers in medical ...*, 2013.

[45] R. L. Hood, T. Ecker, and R. Andriani, “Augmenting convection-enhanced delivery through simultaneous co-delivery of fluids and laser energy with a fiberoptic microneedle device,” *SPIE ...*, 2013.